Uformer-ICS: A U-Shaped Transformer for Image Compressive Sensing Service

Kuiyuan Zhang, Zhongyun Hua, *Senior Member, IEEE*, Yuanman Li, *Member, IEEE*, Yushu Zhang, *Senior Member, IEEE*, and Yicong Zhou, *Senior Member, IEEE*

***Abstract*—Many service computing applications require real-time dataset collection from multiple devices, necessitating efficient sampling techniques to reduce bandwidth and storage pressure. Compressive sensing (CS) has found wide-ranging applications in image acquisition and reconstruction. Recently, numerous deep-learning methods have been introduced for CS tasks. However, the accurate reconstruction of images from measurements remains a significant challenge, especially at low sampling rates. In this article, we propose Uformer-ICS as a novel U-shaped transformer for image CS tasks by introducing inner characteristics of CS into transformer architecture. To utilize the uneven sparsity distribution of image blocks, we design an adaptive sampling architecture that allocates measurement resources based on the estimated block sparsity, allowing the compressed results to retain maximum information from the original image. Additionally, we introduce a multi-channel projection (MCP) module inspired by traditional CS optimization methods. By integrating the MCP module into the transformer blocks, we construct projection-based transformer blocks, and then form a symmetrical reconstruction model using these blocks and residual convolutional blocks. Therefore, our reconstruction model can simultaneously utilize the local features and long-range dependencies of image, and the prior projection knowledge of CS theory. Experimental results demonstrate its significantly better reconstruction performance than state-of-the-art deep learning-based CS methods.**

***Index Terms*—Compressive sensing service, compressive sampling, image reconstruction, adaptive sampling, deep learning.**

Manuscript received 8 July 2023; revised 12 October 2023; accepted 11 November 2023. Date of publication 20 November 2023; date of current version 9 October 2024. This work was supported in part by the National Natural Science Foundation of China under Grants 62071142 and 62001304, in part by the Guangdong Basic and Applied Basic Research Foundation under Grant 2021A1515011406, in part by the Shenzhen Science and Technology Program under Grant ZDSYS20210623091809029, and in part by the Guangdong Provincial Key Laboratory of Novel Security Intelligence Technologies under Grant 2022B1212010005. *(Corresponding author: Zhongyun Hua.)*

Kuiyuan Zhang is with the School of Computer Science and Technology, Harbin Institute of Technology, Shenzhen, Guangdong 518055, China (e-mail: zkyhitsz@gmail.com).

Zhongyun Hua is with the School of Computer Science and Technology, Harbin Institute of Technology, Shenzhen, Guangdong 518055, China, and also with the Guangdong Provincial Key Laboratory of Novel Security Intelligence Technologies, Shenzhen, Guangdong 518055, China (e-mail: huazhongyun@hit.edu.cn).

Yuanman Li is with the Guangdong Key Laboratory of Intelligent Information Processing, College of Electronics and Information Engineering, Shenzhen University, Shenzhen 518060, China (e-mail: yuanmanli@szu.edu.cn).

Yushu Zhang is with the College of Computer Science and Technology, Nanjing University of Aeronautics and Astronautics, Nanjing 210016, China (e-mail: yushu@nuaa.edu.cn).

Yicong Zhou is with the Department of Computer and Information Science, University of Macau, Macau 999078, China (e-mail: yicongzhou@um.edu.mo).

Digital Object Identifier 10.1109/TSC.2023.3334446

I. Introduction

SINCE the advent of the information age, people have increasingly relied on the Internet to transmit, process, and share multimedia data, thereby gradually spurring the development of service computing. The cloud platform provides a seamless way to process and save data through the Internet. However, some service computing applications require real-time data collection from multiple devices [1], [2], necessitating sufficient network bandwidth and storage space. As a result, it's vital to improve the efficiency of data sampling and maintain the data content to reduce network bandwidth and storage space requirements for these applications. Compressive sensing (CS) is an effective signal acquisition technique that can reconstruct a signal using its compressed measurements, which are significantly less than the measurements required by the Nyquist sampling theorem [3], [4]. The sampling process for a signal $\mathbf{x} \in \mathbb{R}^{n\times 1}$ can be expressed as $\mathbf{y} = \mathbf{\Phi x}$, where $\mathbf{\Phi} \in \mathbb{R}^{m\times n}$ is a measurement matrix wherein $n >> m$ and $\mathbf{y} \in \mathbb{R}^{m\times 1}$ comprises the compressed measurements. Because the CS technique can achieve a high compression ratio while maintaining a high reconstruction quality, it can be potentially used in numerous signal acquisition and compression applications [5], [6], especially for tasks involving image signals with high data redundancy [7]. The reconstruction process of CS involves finding solutions for an underdetermined linear system. To achieve high efficiency and accurate reconstruction results, most traditional CS reconstruction algorithms use nonlinear iterations to reconstruct the original signal [8], [9], [10], [11], which is extremely time-consuming. Therefore, these traditional CS methods may not be suitable for real-time applications. Additionally, these traditional CS methods cannot achieve a high reconstruction quality because they lack adaptability to sample signals with varying characteristics.

Some deep learning-based image CS methods have applied convolutional neural networks (CNNs) in the CS task and can achieve both high reconstruction quality and efficiency [12], [13], [14], [15], [16]. These deep learning-based image CS methods use CNN to replace the time-consuming iterative reconstruction process in traditional CS algorithms. They adaptively learn the measurement matrix and reconstruction network using a massive amount of training data. To maintain theoretical interpretability, some of them unfold the traditional CS algorithms into their CS networks using CNNs [14], [16], [17]. However, Owing to the spatial invariance and local inductive biases, CNNs cannot effectively capture long-range dependencies. This results in a limitation to these deep learning-based image CS methods.

Recently, some CS methods [18], [19], [20], [21] have employed the transformer architecture into CS tasks. The transformer has been extremely successful in various language processing [22], [23], [24] and computer vision [25], [26] tasks owing to the robust ability of its self-attention mechanism for capturing long-range dependencies. Inspired by the successful application of transformer, these CS methods [18], [19], [20], [21] utilize the transformer architecture for reconstruction and obtain better performance than previous CNN-based CS methods. While some transformer-based methods [18], [19] also unfold the traditional CS algorithms, their image-level or single-channel level projection cannot make full use of multi-channel feature information in the middle stage. Furthermore, these methods [18], [19], [20], [21] samples all the image blocks at the same sampling ratio without considering the unbalanced block sparsity. These limited correlations between inner CS characteristics and the transformer architecture hinder the further improvement of reconstruction performance.

In this work, we propose a specialized U-shaped transformer architecture for image CS called the Uformer-ICS, which introduces adaptive sampling and projection into the transformer architecture. A natural image usually has uneven sparsity distribution. To utilize the uneven sparsity distribution of image blocks, we design an adaptive sampling architecture that estimates sparsity from image measurements and allocates measurement resources based on the estimated block sparsity. The adaptive sampling model initially samples each image block at a small sampling ratio and estimates the block sparsity according to the measurements. Then it allocates fewer sampling resources to the image block with higher sparsity and vice versa. This approach can make the compressed measurements contain the maximum possible information of the sampled image under a fixed sampling ratio. The image signal is then adaptively sampled block-by-block using a single learnable measurement matrix. Additionally, we introduce a multi-channel projection (MCP) module inspired by traditional CS optimization methods [8], [27]. The original projection operation is applied block-wise on the image domain. To make it suitable for transformer architecture and make full use of multi-channel information, the MCP module adapts projection on the multi-channel feature domain. By integrating the MCP module into the transformer blocks, we construct projection-based transformer blocks, and then build a symmetrical reconstruction model using these blocks and residual convolutional blocks. Therefore, our reconstruction model can simultaneously utilize the local features, and long-range dependencies of image and the prior projection knowledge of CS theory. Our Uformer-ICS is an end-to-end framework that simultaneously learns the sampling and reconstruction processes. Experimental results demonstrate its superior reconstruction performance compared to existing state-of-the-art deep learning-based CS methods.

The main contributions of this study are as follows:

- We propose a new transformer-based network for image CS, called the Uformer-ICS, which effectively introduces two CS characteristics, adaptive sampling and projection, into the transformer architecture.
- We design an adaptive sampling architecture to allocate sampling resources to image blocks based on block sparsity. The block sparsity is estimated from the initial measurements of the sampled image, and we evaluate three sparsity estimation methods in the adaptive sampling architecture.
- We design a MCP module to adapt the projection operation into the multi-channel feature domain, and then develop a symmetrical reconstruction model using a projection-based transformer and residual convolutional blocks, wherein each projection-based transformer block is constructed by integrating the MCP module into the original transformer blocks.
- We conduct extensive experiments to evaluate the proposed Uformer-ICS. The comparison results demonstrate that it outperforms existing state-of-the-art deep learning-based CS methods (as shown in Fig. 1), and the ablation studies validate the effectiveness of the proposed adaptive sampling strategy and the MCP module.

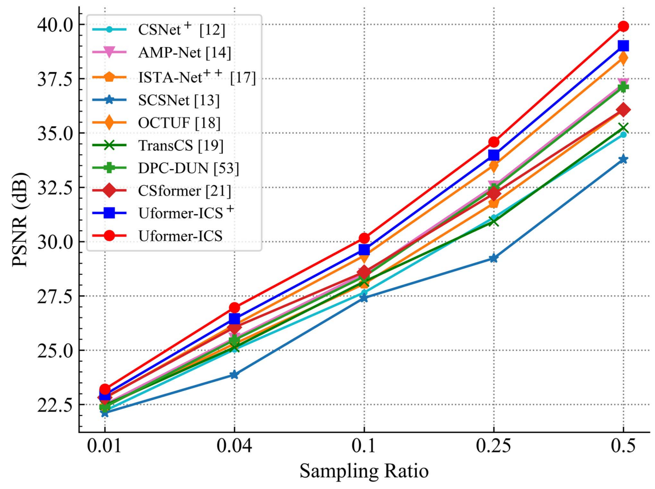

Fig. 1. Average reconstruction performances of the proposed and existing state-of-the-art deep learning-based CS methods. The peak signal-to-noise ratio (PSNR) scores shown are averaged over all images in the five test datasets: Set5, Set11, Set14, BSD100, and Urban100. It is evident that the proposed method achieves significantly better PSNR scores than state-of-the-art deep learning-based CS methods.

The rest of this paper is organized as follows. Section II reviews the traditional CS methods, deep learning-based CS methods, and vision transformers. Section III presents the network structure of the proposed Uformer-ICS. Section IV evaluates the performance of the proposed method and compares it with state-of-the-art methods. Finally, conclusions are drawn in Section V.

II. Related Work

In this section, we present some knowledge of the traditional CS methods, and review existing deep learning-based CS methods and vision transformers.

A. Traditional CS

1) Block-Based CS: The size of the measurement matrix in CS is calculated by multiplying the lengths of the input signal and output measurements. When directly sampling the 1D vector form of a 2D image, the required measurement matrix is considerably large, which results in significantly high memory and computational requirements for the sampling operation. To address this issue, traditional CS algorithms usually sample an image block-by-block [10]. Suppose that each image block $\mathbf{x}_i$ is of size $B \times B$ and the measurement matrix is $\mathbf{\Phi}_B \in \mathbb{R}^{n_B \times B^2}$, where n_B is the number of sampled measurements. The sampling process is expressed as

$$\mathbf{y}_i = \mathbf{\Phi}_B \cdot \mathfrak{T}(\mathbf{x}_i), \tag{1}$$

where $\mathfrak{T}(\mathbf{x}_i)$ denotes the 1D vector form of the image block $\mathbf{x}_i$ and $\mathbf{y}_i \in \mathbb{R}^{n_B \times 1}$ are the measurements of $\mathbf{x}_i$. The sampling ratio (sr) is defined as $sr = n_B/B^2$. Generally, an image block with higher sparsity requires fewer measurements for reconstruction [28]. Therefore, some traditional CS methods improve the reconstruction quality by allocating sampling resources to different blocks [29], [30].

2) Signal Reconstruction: To effectively reconstruct the original signal, some traditional CS methods have developed iterative reconstruction schemes to solve the following optimization problem:

$$\min_{\hat{\mathbf{x}}_i} \frac{1}{2}\|\mathbf{\Phi}_B \mathfrak{T}(\hat{\mathbf{x}}_i) - \mathbf{y}_i\|_2^2 + \mathfrak{R}(\hat{\mathbf{x}}_i), \tag{2}$$

where $\mathfrak{R}(\hat{\mathbf{x}}_i)$ denotes the hand-crafted prior term regarding the structure of the original signal [8], [9], [11], [27]. Each iteration operation includes the following operations:

- *Projection onto the convex set:* Given the reconstruction result $\hat{\mathbf{x}}_i^{(t)}$ of the tth iteration step, this operation uses the gradient descent method to minimize $\|\mathbf{\Phi}_B \mathfrak{T}(\hat{\mathbf{x}}_i) - \mathbf{y}_i\|_2^2$ in (2). Therefore, it can find a vector $\hat{\mathbf{x}}_i^{(t+1)}$ closer to the hyperplane $\mathbf{H} = \{\hat{\mathbf{x}}_i : \mathbf{\Phi}_B \mathfrak{T}(\hat{\mathbf{x}}_i) = \mathbf{y}_i\}$ than $\hat{\mathbf{x}}_i^{(t)}$ without a constraint, e.g., Sparsity constraint. Specifically, the projection operation is calculated as follows:

$$\mathfrak{T}(\hat{\mathbf{x}}_i^{(t+1)}) = \mathfrak{T}(\hat{\mathbf{x}}_i^{(t)}) + \mathbf{\Phi}_B^T(\mathbf{y}_i - \mathbf{\Phi}_B \mathfrak{T}(\hat{\mathbf{x}}_i^{(t)}))/(1+\alpha), \tag{3}$$

  where $\mathbf{\Phi}_B^T(\mathbf{y}_i - \mathbf{\Phi}_B \mathfrak{T}(\hat{\mathbf{x}}_i^{(t)}))$ denotes the gradient of $\|\mathbf{\Phi}_B \mathfrak{T}(\hat{\mathbf{x}}_i) - \mathbf{y}_i\|_2^2$ in (2) and α is the updating step length.
- *Optimizing the prior term:* This operation aims to minimize the hand-crafted prior term $\mathfrak{R}(\hat{\mathbf{x}}_i)$ to constrain the current reconstruction result $\hat{\mathbf{x}}_i^{(t+1)}$. For example, the iterative shrinkage-thresholding algorithm (ISTA) [8] and approximate message passing algorithm (AMP) [27] set the l_1 norm as the prior term to constrain the signal Sparsity, and use a shrinkage/thresholding non-linearity to process $\hat{\mathbf{x}}_i^{(t+1)}$. The denoising-based AMP (DAMP) [31] assumes that the original signal belongs to a certain image class $\mathcal{C}$, and uses a denoiser to project $\hat{\mathbf{x}}_i^{(t+1)}$ onto $\mathcal{C}$.

Despite having good interpretability, traditional CS algorithms suffer from poor reconstruction performance and low efficiency because they cannot adaptively learn the features of the original signal.

B. Vision Transformer

In 2017, the authors of [22] first proposed the transformer for natural language processing tasks. Compared with previous methods based on recurrent neural networks, the transformer has a more powerful ability to model long-range dependencies among tokens using the self-attention mechanism;thus, it can achieve significantly better accuracy and scalability. Specifically, the self-attention layer computes the key-query dot-product among all input tokens. Therefore, its computation complexity grows quadratically with an increase in the number of tokens [22].

To efficiently handle high-resolution images, Vaswani et al. [26] proposed the vision transformer (ViT) that divides an image into non-overlapping patches and employs the transformer to capture dependencies among image patches for image classification tasks. In some low-level vision tasks (e.g., image denoising and image deblocking), an image may be divided into numerous patches, making the computational complexity of ViT extremely high and unacceptable. Considering this, Liu et al. [32] designed a shifted window-based transformer, which applies self-attention in each image window and uses shifted window partitioning to bring connections across windows. Moreover, Zamir et al. [33] proposed a transposed attention scheme that computes the attention map across feature channels. These efforts [32], [33] have significantly reduced the computational complexity of the transformer for image processing tasks, achieving a linear relationship between the computational complexity and the image size.

C. Deep Learning-Based CS

In 2015, the authors of [34] used a deep learning method to solve the signal reconstruction problem and proposed a stacked denoising auto-encoder to reconstruct image patches from their measurements. Inspired by the application of CNNs in image restoration tasks, Kulkarni et al. [35] proposed a deep CNN-based model to implement the non-iterative reconstruction process. These two deep learning-based CS methods directly reconstruct image patches from their measurements [34], [35]. To further improve the reconstruction performance, Shi et al. proposed two end-to-end deep CNN-based models in [12], [36] for image CS, which can simultaneously learn both the sampling and reconstruction processes.

The above CS models directly regard the reconstruction process as a deep learning task without considering the characteristics of CS theory. To improve the interpretability, some studies [14], [16], [37] designed CS networks by unfolding traditional CS algorithms using CNNs. For example, inspired by the traditional ISTA method [8], Zhang et al. [37] proposed a deep network called ISTA-Net by solving the proximal mapping associated with the sparsity-inducing regularizer using nonlinear transformation. The authors of [14] proposed a denoising-based deep CS network called AMP-Net, wherein the reconstruction network unfolds the iterative denoising process of the AMP

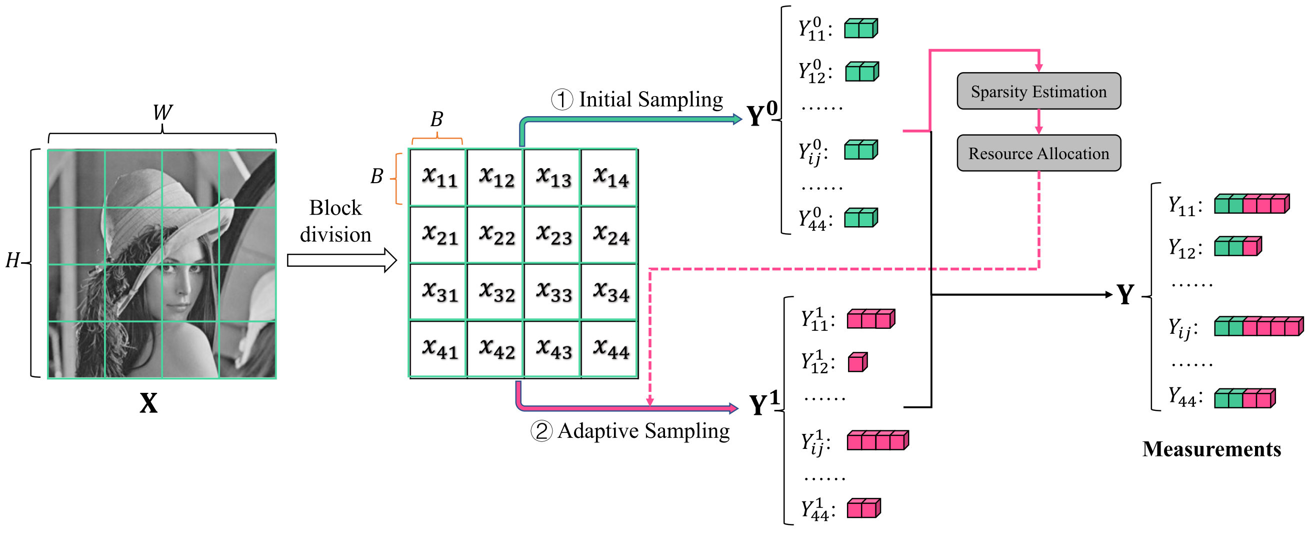
W
H
B
B
X
Block division
x_{11} x_{12} x_{13} x_{14}
x_{21} x_{22} x_{23} x_{24}
x_{31} x_{32} x_{33} x_{34}
x_{41} x_{42} x_{43} x_{44}
① Initial Sampling
② Adaptive Sampling
Y^0
Y^1
Y^0_{11}: Y^0_{12}: …… Y^0_{ij}: …… Y^0_{44}:
Y^1_{11}: Y^1_{12}: …… Y^1_{ij}: …… Y^1_{44}:
Sparsity Estimation
Resource Allocation
Y
Y_{11}: Y_{12}: …… Y_{ij}: …… Y_{44}:
Measurements

Fig. 2. Adaptive sampling model of the proposed Uformer-ICS. First, the image $\mathbf{X}$ is initially sampled, and the initial measurements are utilized to estimate the block sparsity, which is used to adaptively allocate sampling resources for each block. Then, the image is further adaptively sampled block-by-block. The final measurements are obtained by concatenating the initial measurements and adaptive measurements.

algorithm [27] and integrates deblocking modules to eliminate the blocking artifacts.

Recently, some works [18], [19], [20], [21] have employed the transformer architecture on the CS tasks inspired by the successful application of the transformer on vision tasks. The method [20] modified the transformer architecture to fit the patch-to-pixel multi-stage pattern and built a transformer-based hierarchical framework for CS tasks called TCS-Net. Ye et al. [21] proposed a CNN-Transformer hybrid framework to explore the representation capacity of local and global features. To introduce CS characteristics into the transformer architecture, the method [19] builds an ISTA-based transformer backbone that iteratively works with projection operation, and the method [18] fuses the projection operation into a cross attention block. However, they utilize the projection on the image-level or single-channel level, which cannot fully use multi-channel feature information in the middle stage. Moreover, the sparsity in different areas of a natural image usually varies, and these methods [18], [19], [20], [21] sample all image blocks using the same sampling ratio without appropriately considering the uneven sparsity distribution. These insufficient correlations between CS characteristics and the transformer architecture cause a limit to getting further improvement in the reconstruction performance, especially at small sampling ratios.

III. Uformer-ICS

This section details the proposed Uformer-ICS. From an overall perspective, the Uformer-ICS comprises an adaptive sampling model and a reconstruction model. The adaptive sampling model adaptively samples the image block-by-block using a single learnable measurement matrix, and the reconstruction model is a symmetrical U-shaped architecture that reconstructs the original image from the measurements.

To illustrate the sampling and reconstruction processes, we assume that the sampled image is a single-channel image that is denoted as $\mathbf{X} \in \mathbb{R}^{H\times W\times 1}$, where H and W are the height and width of image, respectively, and the block size is $B \times B \times 1$. The vector form of each image block $\mathbf{x}_{ij}$ is represented as $\mathfrak{T}(\mathbf{x}_{ij}) \in \mathbb{R}^{B^2\times 1}$. Herein, $i = \{1, 2, \dots, h\}$ and $j = \{1, 2, \dots, w\}$, where $h = \frac{H}{B}$ and $w = \frac{W}{B}$.

A. Adaptive Sampling Model

The detailed illustration of the adaptive sampling model is shown in Fig. 2. The adaptive sampling model first samples the initial measurements for each image block, then estimates the block sparsity and assign sampling resources, and finally adaptively samples the image.

1) Initial Sampling: It is impossible to access the image before sampling and reconstructing it in some real sampling scenarios. In works [38], [39], the sampling networks directly apply transforms on the image to calculate saliency before sampling it. Therefore, they are limited to tasks that have access to the image before sampling, such as image compression and re-sampling tasks, where the image is already stored on the disk or in memory.

Given the target sampling ratio sr_t for the whole image, we initially sample each image block with a smaller sampling ratio sr_{init} and then adaptively assign the rest sampling resources according to the initial measurements. Assume that the learnable measurement matrix is $\mathbf{\Phi} \in \mathbb{R}^{M\times B^2}$, where M is the maximum number of measurements for each image block. Each image block $\mathbf{x}_{ij}$ is initially sampled as follows:

$$\begin{aligned} n^0 &= \lfloor B^2 * sr_{init} \rfloor \\ \mathbf{y}^0_{ij} &= \mathbf{\Phi}[1 : n^0, :] \cdot \mathfrak{T}(\mathbf{x}_{ij}), \end{aligned} \tag{4}$$

Algorithm 1: Sampling Resources Allocation.

```
Input: Sparsity information $\mathbf{V}$, target sampling ratio $sr_t$, image size $H \times W$, block size $B$, initial number $n^0$ of measurements
Output: measurement number $\mathbf{m}_{ij}$
1:  $h, w = H/B, W/B$
2:  $total = \lfloor sr_t \times H \times W \rfloor$
3:  $rest = total - (n^0 \times h \times w)$
4:  for $i = 1 : h$ do
5:    for $j = 1 : w$ do
6:      $\mathbf{V}_{ij} = \mathbf{V}_{ij} / \mathrm{sum}(\mathbf{V})$
7:      $\mathbf{m}_{ij} = n^0 + \lfloor rest \times \mathbf{V}_{ij} \rfloor$
8:    end for
9:  end for
```

where n^0 is the initial measurement number, $\mathbf{y}_{ij}^0 \in \mathbb{R}^{n^0 \times 1}$ is the initial measurements of the image block $\mathbf{x}_{ij}$.

2) Sparsity Estimation: Because different image blocks have different sparsity, the compressed measurements cannot contain the maximum information of the original image if all image blocks are sampled at the same sampling ratio. Generally speaking, an image block with higher sparsity should be allocated fewer sampling resources because it contains less information.

Before using sparsity estimation methods, we first obtain the initial estimation $\mathbf{x}_{ij}^0$ of each image block

$$\mathbf{x}_{ij}^0 = \mathbf{\Psi}[:, 1 : n^0] \cdot \mathbf{y}_{ij}^0. \tag{5}$$

where $\mathbf{\Psi} \in \mathbb{R}^{B^2 \times M}$ represents the learnable linear mapping matrix. By reshaping and concatenating all $\mathbf{x}_{ij}^0$, a low-quality estimation $\mathbf{X}^0$ is obtained for the input image $\mathbf{X}$.

To estimate the sparsity of the image blocks, we utilize three methods: saliency map (SM), standard deviation (STD), and block difference (DIFF).

Saliency Map: The saliency map method employs discrete cosine transform (DCT) to calculate the saliency information [28], [38], [40]. Specifically, the sparsity information $\mathbf{V}_{ij}$ for each block $\mathbf{x}_{ij}$ is calculated as

$$\begin{aligned}\mathbf{F} &= \mathrm{abs}(\mathrm{C_t}^{-1}(\mathrm{sign}(\mathrm{C_t}(\mathbf{X}^0)))),\\ \mathbf{S} &= \mathbf{G} * \mathbf{F}^2,\\ \mathbf{V}_{ij} &= \sum_{s \in \mathbf{S}_{\mathbf{x}_{ij}}} s \Big/ \sum_{s \in \mathbf{S}} s,\end{aligned} \tag{6}$$

where $\mathrm{C_t}$ and $\mathrm{C_t}^{-1}$ denotes the 2D DCT and its reverse operation, $\mathbf{G}$ is a 2D Gaussian low-pass filter for smoothing, and $\mathbf{S}_{\mathbf{x}_{ij}^0}$ represents the corresponding region for each block $\mathbf{x}_{ij}^0$.

Standard Deviation: The work [30] assumes that an image block $\mathbf{x}_{ij}$ with a larger standard deviation usually has a larger complexity and estimates the standard deviation through the measurements sampled by the Gaussian matrix. Inspired by it, we calculate the standard deviation of each low-quality estimation $\mathbf{x}_{ij}^0$ as the sparsity information $\mathbf{V}_{ij}$ for each block $\mathbf{x}_{ij}$.

Block Difference: The adjacent regions in nature images usually have similar patterns, which benefit the image denoising in the reconstruction. Therefore, the image block having more similar adjacent blocks can be regarded as more sparse and allocated fewer sampling resources. For an image block $\mathbf{x}_{ij}^0$, we first calculate the absolute difference with four adjacent blocks $\{\mathbf{x}_{i,j-1}^0, \mathbf{x}_{i-1,j}^0, \mathbf{x}_{i,j+1}^0, \mathbf{x}_{i+1,j+1}^0\}$, and then average the difference into a scalar as the sparsity information $\mathbf{V}_{ij}$.

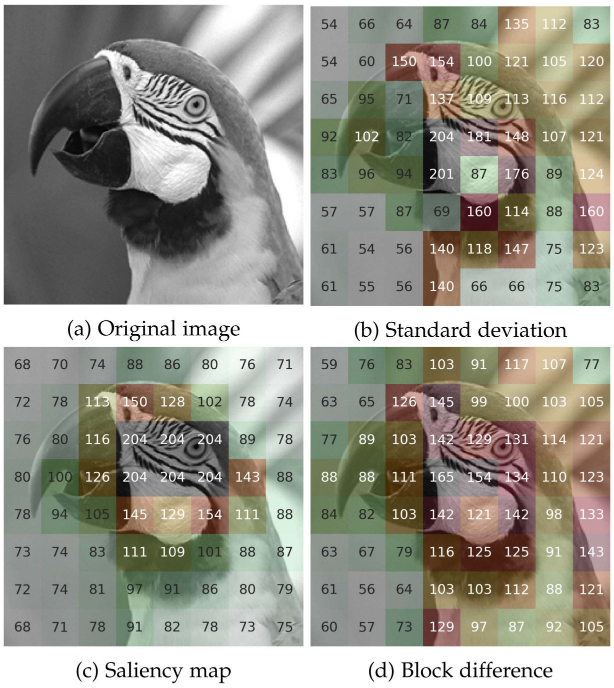

Fig. 3. Measurement allocations using three sparsity estimation methods for the "Parrots" image at the sampling ratio of 0.1.

3) Adaptive Sampling: We assign the rest measurements using the sparsity information $\mathbf{V}_{ij}$ and apply adaptive sampling for each image block. According to the sparsity estimation methods in Section III-A2, the sparsity information $\mathbf{V}_{ij}$ is negatively related to the sparsity. In other words, a larger $\mathbf{V}_{ij}$ means that the corresponding image block $\mathbf{x}_{ij}$ is less sparse and should be allocated more sampling resources.

Algorithm 1 describes the process of allocating sampling resources. The total number of measurements under the target sampling ratio sr_t are first calculated, and the remaining sampling resources are linearly assigned for each image block $\mathbf{x}_{ij}$ based on the sparsity information $\mathbf{V}_{ij}$. Finally, the measurement number $\mathbf{m}_{ij} \in (1, B^2]$ is obtained for each image block $\mathbf{x}_{ij}$.

To better illustrate the adaptive sampling mechanism, we provide one example of the measurement allocations using three sparsity estimation methods for the "Parrots" image shown in Fig. 3. The block size is set to 32×32, and the number on the image block denotes the measurement number. It is evident that image blocks with more complex structures are considered to have less sparsity and are allocated more measurements. For example, the eye in the "Parrots" contains more details and more complex structures; thus, the corresponding image blocks in the eye area are allocated more sampling resources. The upper-left

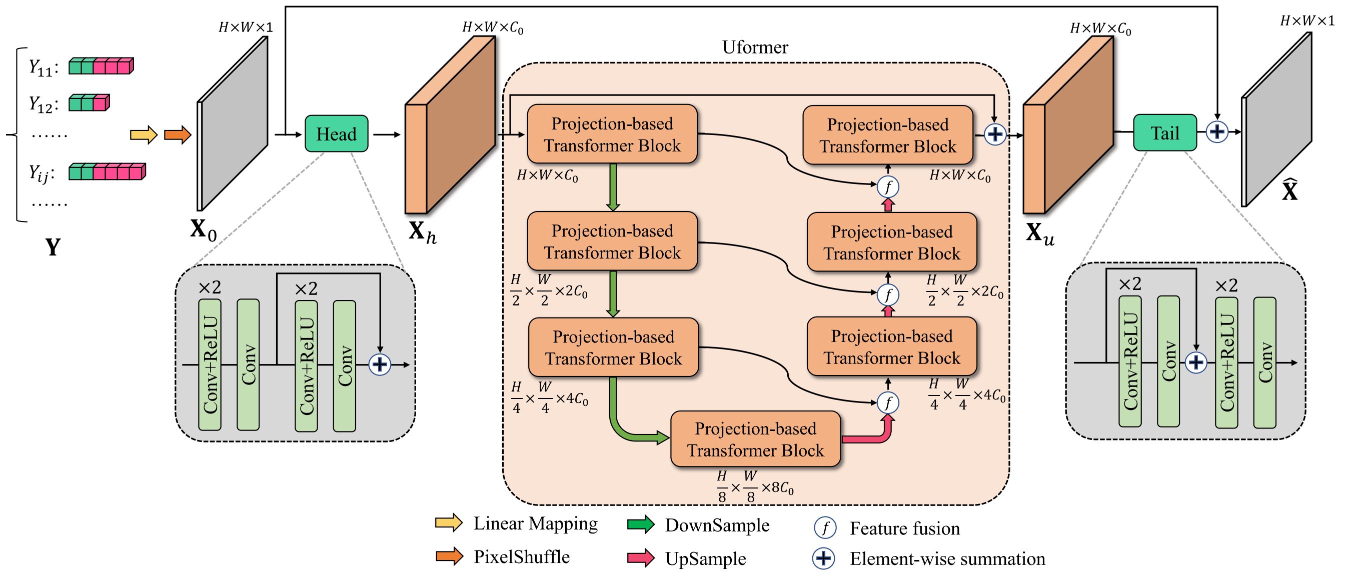

Fig. 4. Overview of the reconstruction model of the proposed Uformer-ICS. Given the adaptive sampling result $\mathbf{Y}$, the reconstruction model first applies linear mapping on it and employs pixel shuffle operation to transform the combined mapping results into an image-like initialization $\mathbf{X}_0$. Then, the reconstruction model feeds the obtained initialization $\mathbf{X}_0$ into the *Head* module for extracting shallow features $\mathbf{X}_h$. Taking $\mathbf{X}_h$ as input, the *Uformer* module captures the long-range dependencies to enhance the feature representation and outputs $\mathbf{X}_u$. Finally, the *Tail* module generates the final reconstruction result $\hat{\mathbf{X}}$ by adding the initialization $\mathbf{X}_0$ and aggregation features of $\mathbf{X}_u$.

and lower-left corners are black backgrounds and therefore are allocated less sampling resources.

Because different image blocks are allocated different measurement numbers, generating a measurement matrix for each possible measurement number results in a significant number of parameters and extremely high memory occupation. To address this problem, we use a scalable sampling strategy that requires only one learnable measurement matrix to sample all image blocks with different measurement numbers. Specifically, we reuse the learnable measurement matrix $\mathbf{\Phi}$ in the initial sampling. Each image block is sampled as follows:

$$\mathbf{y}_{ij}^1 = \mathbf{\Phi}[n^0+1:\mathbf{m}_{ij},:]\cdot\mathfrak{T}(\mathbf{x}_{ij}),$$
$$\mathbf{y}_{ij} = \mathrm{concat}(\mathbf{y}_{ij}^0,\mathbf{y}_{ij}^1), \tag{7}$$

where $\mathbf{y}_{ij}\in\mathbb{R}^{\mathbf{m}_{ij}\times 1}$ is the measurements of the image block $\mathbf{x}_{ij}$. We denote the collection of all measurements $\mathbf{y}_{ij}$ as $\mathbf{Y}$.

B. Reconstruction Model

The overall structure of the reconstruction model is illustrated in Fig. 4. First, the initialization value $\mathbf{X_0}\in\mathbb{R}^{H\times W\times 1}$ of the input image $\mathbf{X}$ is generated by linearly mapping the measurements $\mathbf{Y}$ directly. Specifically, we reuse learnable linear mapping matrix $\mathbf{\Psi}$ in the sparsity estimation, and the image initialization is calculated as:

$$\mathfrak{T}(\hat{\mathbf{x}}_{ij}) = \mathbf{\Psi}[:,1:\mathbf{m}_{ij}]\cdot\mathbf{y}_{ij}$$
$$\mathbf{X_0} = \Xi(\{\hat{\mathbf{x}}_{ij}\}), \tag{8}$$

where Ξ denotes the pixel shuffle operation [41] that repositions elements from the channel dimension to the spatial dimension and we use it to transform the combined linear mapping results into an image-like feature $\mathbf{X_0}$.

Next, the initialization $\mathbf{X}_0$ is processed using a head module H_{head} to extend the channels and extract the local shadow features $\mathbf{X}_h\in\mathbb{R}^{H\times W\times C_0}$, where C_0 is the number of channels. The Uformer module then captures the long-range features from $\mathbf{X}_h$ to obtain a feature $\mathbf{X}_u$. Finally, a tail module H_{tail} aggregates $\mathbf{X}_u$ to produce a residual reconstruction result, and the final reconstruction result $\hat{\mathbf{X}}$ is generated by adding the initialization $\mathbf{X}_0$ and the residual reconstruction result.

In the subsequent subsections, the head and tail modules are first illustrated and then the Uformer module is described in detail.

C. Head & Tail Modules

As shown in Fig. 4, the head module H_{head} comprises several convolutional layers and a residual convolutional block. After obtaining the initialization result $\mathbf{X_0}$, the H_{head} enlarges the channels further and extracts local shallow features from $\mathbf{X_0}$ as follows:

$$\mathbf{X}_h = H_{head}(\mathbf{X_0}), \tag{9}$$

where $\mathbf{X}_h$ is of size $H\times W\times C_0$.

To ensure symmetry with the head module H_{head}, the tail module H_{tail} stacks a residual convolutional block and several convolutional layers. Given output $\mathbf{X}_u$ of the Uformer module, the H_{tail} aggregates the features of $\mathbf{X}_u$ to obtain the final reconstruction result $\hat{\mathbf{X}}$ as follows:

$$\hat{\mathbf{X}} = H_{tail}(\mathbf{X}_u)+\mathbf{X_0}, \tag{10}$$

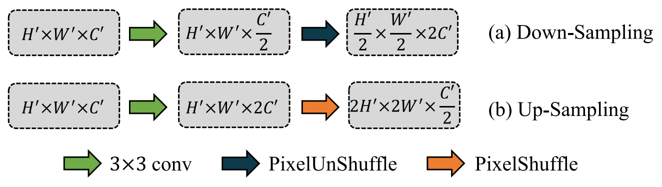

Fig. 5. Illustrations of the feature down-sampling and up-sampling operations.

where $\hat{\mathbf{X}}$ is of size $H \times W \times 1$, and the residual learning [42] is applied to improve the convergence speed and reconstruction performance of the proposed model.

D. Uformer

As illustrated in Fig. 4, the Uformer is a U-shaped four-level hierarchical encoder-decoder. To introduce the prior knowledge of CS into the transformer architecture, we propose a multi-channel projection (MCP) and integrate it into the stacked transformer blocks to develop the projection-based transformer block. In the following sections, we will illustrate the overall pipeline of the Uformer and present its components in detail.

1) Pipeline: Based on the common design of the U-shaped structure [43], the output $\mathbf{X}_h$ of the head module is first passed through four encoder levels. The resolutions of feature maps are gradually reduced from the top to the bottom levels using feature down-sampling operations shown in Fig. 5(a). We employ a 3×3 convolutional layer and pixel unshuffle operation [41] to double the number of channels and reduce the resolution by 50%. Therefore, the ith level of the encoder produces a feature map of size $\frac{H}{2^i} \times \frac{W}{2^i} \times 2^i C_0$, where $i \in [0, 1, 2, 3]$.

The decoder progressively recovers the high-resolution features by using the low-resolution feature map from the lowest encoder level as its input. Fig. 5(b) shows the feature up-sampling operation. We employ a 3×3 convolutional layer and pixel shuffle operation [41] to reduce the channels by 50% and double the resolution. Moreover, the features obtained on the decoder side are fused with the encoder features to enhance the feature representation.

2) Window-Based Self-Attention: The computational complexity of the original self-attention layer in the transformer increases quadratically with image size. In this study, the window-based multi-head self-attention (W-MSA) [32] is used to reduce the computational complexity because it computes self-attention in non-overlapping windows and its computational complexity increases linearly with image size. Given an input feature map $\mathbf{Z} \in \mathbb{R}^{H' \times W' \times d}$, the W-MSA divides it into non-overlapping windows of size $W \times W \times d$. Suppose that $\mathbf{P} \in \mathbb{R}^{W^2 \times d}$ denotes the W^2 pixels in a window, the W-MSA applies the self-attention process to these pixels as follows:

$$\mathbf{Q}, \mathbf{K}, \mathbf{V} = \mathbf{P}\mathbf{W}_q, \mathbf{P}\mathbf{W}_k, \mathbf{P}\mathbf{W}_v,$$
$$\text{Attention}(\mathbf{Q}, \mathbf{K}, \mathbf{V}) = \text{SoftMax}\left(\mathbf{Q}\mathbf{K}^T/\sqrt{d} + \mathbf{B}\right)\mathbf{V}, \quad (11)$$

where $\mathbf{W}_q, \mathbf{W}_v, \mathbf{W}_v \in \mathbb{R}^{d \times d}$ are the *query, key*, and *value* projection matrices, respectively, $\mathbf{Q}, \mathbf{K}, \mathbf{V}$ denote the *query, key* and *value* results, respectively, and $\mathbf{B} \in \mathbb{R}^{(2W^2-1)\times(2W^2-1)}$ denotes the learnable relative position bias. The attention results are transformed into a feature map with the same size as $\mathbf{Z}$. It should be noted that we omit the multi-head format in (11) for simplicity. Besides, we also use the shifted window partitioning scheme [32] to capture dependencies across windows, and the W-MSA with shifted window partitioning is referred to SW-MSA.

3) Multi-Channel Projection: The projection operation reuses the measurement matrix to make the current image reconstruction more similar to the ground truth image, which can well utilize the prior knowledge of CS during the reconstruction process. It is necessary to integrate this CS characteristic into the transformer to achieve high performance. As shown in (3), the projection operation updates each image block with a single channel. However, the features in a transformer architecture generally have smaller resolutions but much more channels than the single-channel image. Therefore, the projection operation cannot be directly applied to the transformer architecture.

To address this issue, we propose the multi-channel projection (MCP), which is derived from the original projection operation expressed in (3) but applies block-wise projection on the multi-channel feature domain. The details of MCP are shown in Fig. 6. Specifically, MCP first reshapes the input feature into an image-like feature $\mathbf{X}' \in \mathbb{R}^{H \times W \times C'}$ using the pixel shuffle operation [41], ensuring that it has the same resolution as the input image. Thereafter, MCP applies block-wise projection to each block of each channel of $\mathbf{X}'$ feature using the learnable measurement matrix $\mathbf{\Phi}$ and the adaptive sampling results $\mathbf{Y}$. The block-wise projection operation on each channel is calculated as follows:

$$\mathbf{y}'_{ij,c} = \mathbf{y}_{ij} - \mathbf{\Phi}[1:\mathbf{m}_{ij},:]\mathfrak{T}(\mathbf{x}'_{ij,c})$$
$$\mathfrak{T}(\mathbf{x}''_{ij,c}) = \mathfrak{T}(\mathbf{x}'_{ij,c}) + \mathbf{\Phi}[1:\mathbf{m}_{ij},:]^T\mathbf{y}'_{ij,c}/(1+\boldsymbol{\alpha}_c), \quad (12)$$

where $c \in \{1, \ldots, C'\}$ is the channel index of $\mathbf{X}'$, $\mathfrak{T}(\mathbf{x}'_{ij,c})$ denotes the 1D vector form of each block $\mathbf{x}'_{ij,c}$ in the cth channel of $\mathbf{X}'$, $\mathbf{m}_{ij}$ represents the measurement number of each block in the sampling process, and updating step $\boldsymbol{\alpha} \in \mathbb{R}^{C'}$ is set to be learnable. By combining and reshaping the block-wise projection results, we can also obtain a feature $\mathbf{X}''$ with the same shape as $\mathbf{X}'$. Finally, MCP applies the pixel unshuffle operation to $\mathbf{X}''$ for restoring its channel number and original resolution.

4) Projection-Based Transformer Block: After constructing the MCP module for the transformer architecture, we develop a projection-based transformer block by integrating the MCP module into the transformer architecture. Fig. 6 shows the structure of the projection-based transformer block. Given the input feature $\mathbf{F}_{input}$, the entire process of the projection-based transformer block can be formulated as

$$\mathbf{Z}^{(0)} = \mathbf{F}_{input}$$
$$\mathbf{Z}^{(k)} = \text{WTB}(\mathbf{Z}^{(k-1)}), \quad k = 1, \ldots, L$$
$$\mathbf{F}_{output} = \text{MCP}(\text{LN}(\mathbf{Z}^{(L)})), \quad (13)$$

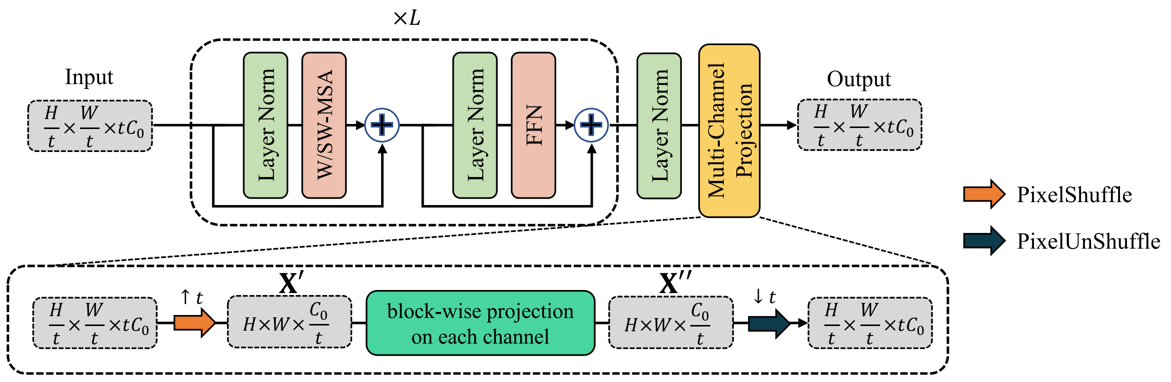
×L
Input
$\frac{H}{t}\times\frac{W}{t}\times tC_0$
Layer Norm
W/SW-MSA
Layer Norm
FFN
Layer Norm
Multi-Channel Projection
Output
$\frac{H}{t}\times\frac{W}{t}\times tC_0$
PixelShuffle
PixelUnShuffle
$\uparrow t$
X′
$H\times W\times\frac{C_0}{t}$
block-wise projection on each channel
X″
$H\times W\times\frac{C_0}{t}$
$\downarrow t$
$\frac{H}{t}\times\frac{W}{t}\times tC_0$

Fig. 6. Structure of the projection-based transformer block. First, L Transformer blocks are stacked to learn long-range dependencies, and then the multi-channel projection module is used to update the multi-channel features block-wise.

where LN represents the layer normalization [44], and WTB indicates the following calculation process of an original transformer block:

$$\mathbf{T}^{(k)} = \mathbf{Z}^{(k-1)} + \text{W/SW-MSA}(\text{LN}(\mathbf{Z}^{(k-1)}))$$
$$\mathbf{Z}^{(k)} = \mathbf{T}^{(k)} + \text{FFN}(\text{LN}(\mathbf{T}^{(k)})), \tag{14}$$

where FFN denotes a feed-forward network containing two fully connected layers. Following the shifted window partitioning scheme [32], the W-MSA is used when k is odd and SW-MSA is used when k is even. Because the MCP module reuses the learnable measurement matrix and only introduces a learnable updating step $\boldsymbol{\alpha}$, the projection-based transformer block can exploit the prior knowledge of CS with a small computation overhead and little extra parameters compared to original stacked transformer blocks.

5) Feature Fusion: The encoder features are fused on the decoder side to enhance the feature representation. Given two features of the same size, they are directly concatenated in the channel dimension and a 1×1 convolutional layer is used to reduce the number of channels in the concatenation result by 50%. Thereafter, a residual convolutional block is employed to further improve the feature fusion ability. Therefore, the feature fusion result has the same size as each input feature.

E. Loss Function

Following the settings of existing CS methods [12], [14], we use the mean square error (MSE) to calculate the loss. The loss function of the proposed model comprises three parts $\mathcal{L}_1$, $\mathcal{L}_2$ and $\mathcal{L}_3$.

Let $\{\mathbf{X}_k\}_{k=1}^{N}$ represent a training set. We first use the MSE to measure the difference between the input images and their corresponding reconstructed images as follows:

$$\mathcal{L}_1 = \frac{1}{2N}\sum_{k=1}^{N}\|\hat{\mathbf{X}}_k - \mathbf{X}_k\|_2^2, \tag{15}$$

where $\hat{\mathbf{X}}_k$ denotes the reconstructed image of the kth input image $\mathbf{X}_k$. Inspired by the cycle-consistent loss [45], we also use the MSE to measure the difference between the measurements of the input images and the measurements of their corresponding reconstructed images as follows:

$$\mathcal{L}_2 = \frac{1}{2\,N}\sum_{k=1}^{N}\sum_{i=1}^{h}\sum_{j=1}^{w}\|y_{kij} - \mathbf{\Phi}[1:\mathbf{m}_{kij},:]\mathfrak{T}(\hat{\mathbf{x}}_{kij})\|_2^2, \tag{16}$$

where $\mathfrak{T}(\hat{\mathbf{x}}_{kij})$ denotes the 1D vector form of the image block $\hat{\mathbf{x}}_{kij}$ in the reconstructed image $\hat{\mathbf{X}}_k$. Considering that sparsity estimation is based on low-quality estimation of image, we further add an additional loss item to improve the accuracy of sparsity estimation

$$\mathcal{L}_3 = \frac{1}{2\,N}\sum_{k=1}^{N}\|\hat{\mathbf{X}}_k^0 - \mathbf{X}_k\|_2^2, \tag{17}$$

where $\hat{\mathbf{X}}_k^0$ is the low-quality estimation of image $\mathbf{X}_k$.

Finally, we define the total loss of the proposed model as

$$\mathcal{L} = \mathcal{L}_1 + \lambda_1 \cdot \mathcal{L}_2 + \lambda_2 \cdot \mathcal{L}_3, \tag{18}$$

where λ_1 and λ_2 are the regularization weights, which are set to 0.1 by default.

IV. Performance Evaluation

A. Experimental Settings

1) Datasets: Compared to pure CNN models, a transformer model needs to be trained using a much larger training set [26]. To thoroughly evaluate the performance of the proposed model, we randomly select 40,000 images from the COCO 2017 Unlabeled Images dataset[1] [46] as the training dataset and 100 images as the validation dataset. We conduct experiments to evaluate all the CS methods over five commonly used datasets: Set5 [47], Set11 [35], Set14 [48], BSD100 [49], and Urban100 [50]. For all used datasets, we only utilize the Y channel in the YCbCr color space of each color image.

2) Implementation Details: The image block size in the sampling process is set to $B = 32$. Given the target sampling ratio sr_t, the initially sampling ratio sr_{init} is set to $sr_t/2$ when $sr_t <= 0.1$ and to $sr_t/3$ when $sr_t > 0.1$. The maximum sampling ratio $sr_{\max}$ for any image block is $max(1.0, 2sr_t)$.

[1]https://cocodataset.org

The number of channels in the head module is set to $C_0 = 32$. From the top to the bottom levels of the Uformer, the number L of the attention layers and FFN layers in the projection-based transformer block is set as [4, 4, 6, 6], the number of heads in W/SW-MSA is set as $[1, 2, 4, 8]$, and the window sizes in W/SW-MSA are set to $[8, 8, 4, 4]$.

We train the proposed Uformer-ICS for a maximum of 100 epochs at each sampling ratio. Early-stopping is used to suspend training when there is no PSNR improvement on the validation set after the 50th epoch. The batch size is set to 16. For each input image in the training process, we first randomly flip and rotate it to augment the image features and then randomly crop the augmentation result into a sub-image of size 128×128 for training. We use the Adam optimizer [51] to optimize the parameters. The learning rate is initialized at 0.0001 and then decayed to half if there is no PSNR improvement on the validation dataset for five epochs in the training process. We use PyTorch framework to implement our models and conduct all the experiments on a computer with a RTX4090 GPU and an Intel i9-10920X CPU. It takes about 7 minutes to train one epoch. Our codes are available at Github.[2]

3) Sampling and Reconstruction Using One Model: The proposed model can also sample and reconstruct images at arbitrary sampling ratios with only one-time training, which can significantly reduce the training time and storage burden. In our implementation, we term the proposed model with only one-time training for arbitrary sampling ratios as Uformer-ICS$^+$. In the training process of Uformer-ICS$^+$, each image in the training set is randomly assigned a target sampling ratio ranging from 0.01–0.5. Besides the training strategy, Uformer-ICS+ and Uformer-ICS have different sizes of the measurement matrices. The size of measurement matrix of Uformer-ICS is $(B^2 \cdot sr_{\max}) \times B^2$, while that of Uformer-ICS$^+$ is $B^2 \times B^2$ to deal with different sampling tasks at varying sr_t. We test the performances of both kinds of models in our experiments.

4) Competing Methods: We compare our method with eight deep learning-based CS methods, which are developed using CNNs or Transformers and have shown state-of-the-art reconstruction performances.

- SCSNet [13]: This is a scalable sampling network that shares a single learnable measurement matrix for multiple reconstruction models.
- CSNet$^+$ [12]: This network utilizes several residual convolutional blocks for image reconstruction.
- ISTA-Net^{++} [17]: This scalable sampling network uses multiple non-learnable sampling matrices but only a single deep-unfolding multi-stage network.
- AMP-Net [14]: This is a deep-unfolding multi-stage network, which unfolds the traditional AMP method [27] and integrates deblocking modules to eliminate blocking artifacts.
- OCTUF [18]: This work utilize optimization-inspired cross-attention transformer module to construct a lightweight unfolding framework for image CS.

[2]https://github.com/RedamancyAY/Uformer-ICS

TABLE I
ABLATION STUDIES ON SPARSITY ESTIMATION METHODS

sr	Non Adaptive	Sparsity Estimation Methods		
		STD	DIFF	SM
0.01	**22.06**/21.86	21.95/21.92	22.01/**21.96**	22.04/21.94
0.04	26.61/25.76	26.89/26.03	**27.03**/26.28	26.90/**26.29**
0.1	30.43/29.45	30.52/29.57	**30.73**/29.87	30.41/**30.00**
0.25	34.48/33.93	34.24/34.17	**34.85**/34.55	34.55/**34.89**
0.5	38.35/38.45	38.54/39.20	39.10/39.69	**39.28**/**40.33**
Avg.	30.39/29.89	30.43/30.18	**30.74**/30.47	30.64/**30.69**

We list the PSNR results on Set11/Urban100 datasets at different sampling ratios (sr).

- TransCS [19]: This Transformer-CNN hybrid network contains a customized ISTA-based transformer backbone to model long-distance dependence and a auxiliary CNN to capture the local features.
- CSformer [21]: This hybrid network utilizes two stems to integrate the CNN and transformer architectures for improved representation learning.
- DPC-DUN [52]: This deep unfolding network introduces a path-controllable selector to dynamically select a rapid and appropriate route for each image.

To keep consistency with other models, we set all the sampling matrices learnable for ISTA-Net^{++} [17] and DPC-DUN [52]. Additionally, four traditional CS methods, the TV [9], BCS-FOCUSS [11], DAMP [31], and MH-BCS-SPL [53], are also compared to demonstrate the powerful learning ability of the deep learning-based CS methods. We evaluate all of these methods using their publicly available implementation codes and retrain the deep-learning models on our constructed COCO-40000 training set.

B. Ablation Studies

In this section, we conduct ablation studies on several components of the proposed Uformer-ICS to investigate their effectiveness and select the best settings.

1) Adaptive Sampling and Sparsity Estimation Methods: A natural image usually contains different sparsities in different image blocks. To retain more information of the original image in the compressed measurements, we use an adaptive sampling strategy to sample image blocks based on their sparsity. To estimate the block sparsity of the sampled image, we utilize three methods: SM, STD, and DIFF. Besides, to demonstrate the effectiveness of the adaptive sampling strategy, we build a non-adaptive model by discarding the adaptive sampling strategy from the proposed Uformer-ICS and train it by sampling each image block equally.

Table I shows the testing results of the adaptive and non-adaptive models on Set11 and Urban100 datasets at five sampling ratios $\{0.01, 0.04, 0.1, 0.25, 0.5\}$. As can be seen, our models using any sparsity estimation methods can obtain better reconstruction quality than the non-adaptive model. Compared to the non-adaptive model, the average PSNR results on Urban100 on five sampling ratios $\{0.01, 0.04, 0.1, 0.25, 0.5\}$ can

TABLE II
ABLATION STUDY RESULTS OF THE PROPOSED UFORMER-ICS ON SET11 AND URBAN100 DATASETS AT DIFFERENT SAMPLING RATIOS (sr)

Setting	MCP	Feature Fusion	$\mathcal{L}_2$	Different sr on Set11					Different sr on Urban100					Parameters
				0.01	0.04	0.1	0.25	0.5	0.01	0.04	0.1	0.25	0.5	
(a)	×	"concat"	✓	21.94	26.64	29.27	33.39	38.68	21.67	25.54	28.56	32.59	37.86	9.1588M
(b)	✓	"add"	✓	21.97	**26.94**	30.68	34.54	**39.38**	21.94	26.27	29.99	34.86	40.07	9.1159M
(c)	✓	"concat"	×	21.99	26.75	**30.73**	34.49	38.57	**21.96**	26.23	29.99	34.68	40.09	9.1589M
(d)	✓	"concat"	✓	**22.04**	26.90	30.41	**34.55**	39.28	21.94	**26.29**	**30.00**	**34.89**	**40.33**	9.1589M

For the feature fusion, "concat" denotes the concatenation operation and "add" indicates the skip connection.

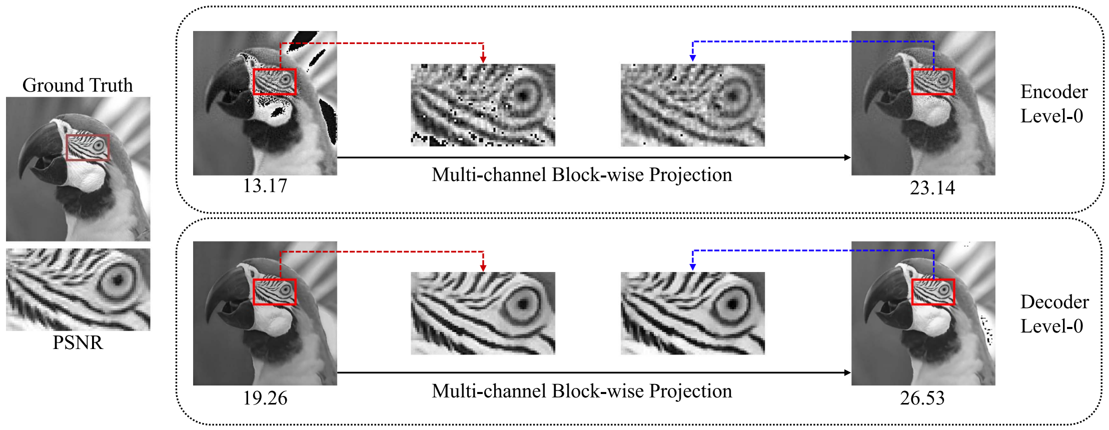
Ground Truth
PSNR
13.17
Multi-channel Block-wise Projection
23.14
Encoder Level-0
19.26
Multi-channel Block-wise Projection
26.53
Decoder Level-0

Fig. 7. Visual effects of the proposed multi-channel projection (MCP) modules at the sampling ratio of 0.1. It applies multi-channel block-wise projection to the input feature map for feature updating. Note that we only extract the image feature maps before and after the MCP modules for comparison, and we utilize the tail module H_{tail} to convert these multi-channel feature maps into single-channel images for visualization.

be improved by 0.29 dB, 0.58 dB, and 0.80 dB for the adaptive models when using STD, DIFF, and SM, respectively.

In conclusion, the adaptive sampling strategy can effectively improve the reconstruction quality. Besides, the sparsity estimation method SM can lead to better reconstruction quality than STD and DIFF on the whole, especially in the large dataset Urban100. This is because the DCT used by the SM method can allow it to accurately capture the image's energy distribution and exhibit greater robustness to noise compared to the STD and DIFF methods. Therefore, the SM method can better estimate the sparsity in our model. In the next sections, we use the SM to estimate sparsity by default if there are no special instructions.

For the proposed reconstruction model, we construct the Uformer architecture to utilize the long-range dependency capture ability. Considering that CS characteristics are crucial for image reconstruction in CS tasks [14], [16], we develop a projection-based Transformer block to introduce the prior projection knowledge of CS into the transformer architecture. As shown in Fig. 6, we integrate the MCP module into the original stacked Transformer blocks to construct the projection-based transformer block. Because the MCP reuses the measurement matrix and the measurements to update the image block, it can introduce the CS characteristics into the transformer architecture. Additionally, it brings in little computation overhead and few extra parameters by introducing only a learnable updating step vector. As can be seen from the settings (a) and (d) in Table II, the MCP only increases the model parameters from 9.1588 M to 9.1589 M.

2) Multi-Channel Projection: To evaluate the effectiveness of the MCP, we remove all the MCP modules in the projection-based transformer block to test the reconstruction performance. As shown in Table II, without the MCP modules, the PSNR scores will drop by approximately 0.1∼1.17 dB and 0.24∼2.47 dB on Set11 and Urban100 datasets, respectively, thereby demonstrating the importance of our MCP module for image reconstruction.

In addition, Fig. 7 presents the visualization results of the feature maps in the MCP modules of the proposed Uformer-ICS. The sampling ratio is set to 0.1. Note that we use the tail module H_{tail} to convert the multi-channel feature maps into single-channel images for visualization. It can be observed that the projection results have finer details and clearer edges than the input feature maps. The quantitative results in Table II and the visual results in Fig. 7 verify the effectiveness of the multi-channel projection.

3) Feature Fusion: In the proposed model, we use the concatenation operation for feature fusion to aggregate the encoder features on the decoder side. In addition to the concatenation operation, another commonly used feature fusion method is the skip connection [42], which directly adds the features of the two input branches element-wise. As can be seen from Table II, the reconstruction performances of the concatenation

TABLE III
QUANTITATIVE PERFORMANCE COMPARISONS OF THE PROPOSED UFORMER-ICS AND UFORMER-ICS$^+$ WITH EXISTING CS METHODS UNDER MULTIPLE SAMPLING RATIOS (sr)

Dataset	Methods	sr (PSNR/SSIM)				
		0.01	0.04	0.1	0.25	0.5
Set5	TV [9]	16.84/0.4412	21.34/0.5554	25.88/0.7239	30.96/0.8712	36.22/0.9465
	BCS-FOCUSS [11]	16.79/0.4787	23.13/0.6549	27.30/0.7658	31.84/0.8693	36.26/0.9340
	BM3D-DAMP [31]	6.48/0.0080	14.70/0.4573	24.11/0.6849	31.24/0.8752	37.89/0.9461
	MH-BCS-SPL [53]	14.59/0.3812	24.10/0.6709	28.66/0.8108	32.94/0.8975	36.99/0.9467
	SCSNet [13]	22.58/0.5565	24.21/0.6552	28.65/0.8070	30.20/0.8862	34.79/0.9532
	ISTA-Net^{++} [17]	24.17/0.6600	29.09/0.8297	33.09/0.9065	37.03/0.9502	40.90/0.9747
	AMP-Net [14]	24.65/0.6699	29.51/0.8394	33.63/0.9150	37.56/0.9564	41.93/0.9800
	CSNet$^+$ [12]	24.03/0.6461	28.72/0.8154	32.47/0.9013	36.17/0.9469	39.64/0.9735
	OCTUF [18]	24.89/0.6901	30.05/0.8537	34.37/0.9234	38.37/0.9598	43.09/0.9826
	TransCS [19]	24.32/0.6644	28.99/0.8235	33.29/0.9042	35.92/0.9351	39.39/0.9694
	DPC-DUN [52]	24.33/0.6636	29.28/0.8397	33.51/0.9169	37.39/0.9576	41.79/0.9803
	CSformer [21]	24.65/0.6948	29.69/0.8520	33.33/0.9154	37.10/0.9551	40.97/0.9783
	Uformer-ICS$^+$	24.89/0.6932	30.40/0.8572	34.61/0.9238	38.80/0.9602	43.68/0.9811
	Uformer-ICS	25.15/0.7025	30.76/0.8637	34.97/0.9265	39.23/0.9612	44.43/0.9824
Set11	TV [9]	15.49/0.3800	19.25/0.4988	22.78/0.6592	27.64/0.8296	32.81/0.9264
	BCS-FOCUSS [11]	17.58/0.4488	20.96/0.5856	24.06/0.7075	28.41/0.8359	33.17/0.9203
	BM3D-DAMP [31]	5.18/0.0076	13.84/0.3904	21.21/0.6070	28.29/0.8484	35.19/0.9429
	MH-BCS-SPL [53]	12.82/0.3205	21.49/0.6218	26.01/0.7862	30.53/0.8891	34.94/0.9447
	ISTA-Net^{++} [17]	21.23/0.5699	25.34/0.7640	28.83/0.8643	32.67/0.9316	36.65/0.9681
	SCSNet [13]	20.71/0.5478	22.42/0.6784	27.37/0.8454	28.36/0.8881	33.29/0.9542
	AMP-Net [14]	21.09/0.5734	25.53/0.7759	29.13/0.8740	33.04/0.9414	36.74/0.9735
	CSNet$^+$ [12]	20.98/0.5553	24.91/0.7503	28.40/0.8575	32.14/0.9252	33.79/0.9643
	OCTUF [18]	21.74/0.5946	26.52/0.8001	30.21/0.8906	34.31/0.9499	38.13/0.9767
	TransCS [19]	21.30/0.5674	24.58/0.7541	28.42/0.8601	30.38/0.9102	33.53/0.9563
	DPC-DUN [52]	21.13/0.5753	25.37/0.7778	29.05/0.8749	32.58/0.9422	36.89/0.9742
	CSformer [21]	21.90/0.6073	26.09/0.7989	29.02/0.8791	32.20/0.9430	35.40/0.9714
	Uformer-ICS$^+$	21.62/0.5993	26.36/0.8031	30.07/0.8911	34.37/0.9486	38.55/0.9740
	Uformer-ICS	22.04/0.6130	26.90/0.8173	30.41/0.9003	34.55/0.9522	39.28/0.9768
Set14	TV [9]	17.01/0.4025	20.82/0.5008	24.32/0.6456	28.48/0.7988	33.35/0.9071
	BCS-FOCUSS [11]	18.32/0.4586	21.99/0.5716	25.26/0.6816	29.01/0.8082	33.19/0.9023
	BM3D-DAMP [31]	6.17/0.0076	15.08/0.4032	22.73/0.5794	28.18/0.7630	34.29/0.8901
	MH-BCS-SPL [53]	14.36/0.3383	22.65/0.5878	26.63/0.7308	30.46/0.8489	34.49/0.9243
	ISTA-Net^{++} [17]	23.03/0.5770	26.54/0.7114	29.49/0.8153	33.20/0.9022	37.23/0.9549
	SCSNet [13]	22.58/0.5565	24.21/0.6552	28.65/0.8070	30.20/0.8862	34.79/0.9532
	AMP-Net [14]	23.23/0.5804	26.83/0.7202	29.95/0.8277	33.93/0.9158	38.51/0.9642
	CSNet$^+$ [12]	22.74/0.5619	26.09/0.7012	29.02/0.8117	32.52/0.9009	36.20/0.9556
	OCTUF [18]	23.45/0.5909	27.29/0.7333	30.52/0.8392	34.76/0.9237	39.64/0.9684
	TransCS [19]	23.03/0.5708	26.24/0.7029	29.25/0.8174	31.83/0.8934	36.04/0.9541
	DPC-DUN [52]	22.95/0.5769	26.64/0.7206	29.79/0.8269	33.72/0.9174	38.34/0.9648
	CSformer [21]	23.52/0.5954	27.10/0.7357	29.75/0.8327	33.49/0.9187	37.36/0.9635
	Uformer-ICS$^+$	23.73/0.5987	27.58/0.7381	30.89/0.8405	35.15/0.9218	39.68/0.9645
	Uformer-ICS	24.00/0.6059	27.95/0.7474	31.28/0.8461	35.68/0.9253	40.48/0.9669
BSD100	TV [9]	17.63/0.4174	21.26/0.5054	24.68/0.6249	27.93/0.7719	31.97/0.8920
	BCS-FOCUSS [11]	19.10/0.4587	22.89/0.5625	25.25/0.6566	28.22/0.7795	31.86/0.8834
	BM3D-DAMP [31]	6.79/0.0065	15.84/0.4096	23.06/0.5513	26.97/0.6979	31.02/0.8265
	MH-BCS-SPL [53]	15.38/0.3614	23.15/0.5645	25.72/0.6754	28.98/0.8049	32.65/0.9004
	ISTA-Net^{++} [17]	23.89/0.5540	26.29/0.6697	28.58/0.7763	31.80/0.8798	35.84/0.9481
	SCSNet [13]	23.64/0.5424	25.44/0.6382	28.30/0.7732	30.64/0.8743	35.22/0.9535
	CSNet$^+$ [12]	23.70/0.5456	26.15/0.6643	28.39/0.7752	31.49/0.8810	35.49/0.9530
	AMP-Net [14]	23.93/0.5544	26.46/0.6765	28.88/0.7882	32.38/0.8952	36.90/0.9601
	OCTUF [18]	24.09/0.5627	26.71/0.6870	29.23/0.7976	32.83/0.9001	37.72/0.9647
	TransCS [19]	23.90/0.5494	26.24/0.6648	28.70/0.7803	31.50/0.8768	35.63/0.9511
	DPC-DUN [52]	23.82/0.5538	26.41/0.6779	28.83/0.7895	32.39/0.8987	36.89/0.9613
	CSformer [21]	23.95/0.5642	26.60/0.6909	28.79/0.7923	32.17/0.8975	36.44/0.9613
	Uformer-ICS$^+$	24.27/0.5660	27.13/0.6948	29.74/0.8041	33.67/0.9031	38.74/0.9623
	Uformer-ICS	24.39/0.5697	27.30/0.7013	29.89/0.8065	33.90/0.9049	39.26/0.9647
Urban100	TV [9]	16.17/0.3819	19.31/0.4766	22.07/0.6181	26.05/0.7889	31.06/0.9107
	BCS-FOCUSS [11]	16.68/0.4116	20.17/0.5279	22.89/0.6435	26.65/0.7864	31.19/0.8947
	BM3D-DAMP [31]	6.13/0.0065	14.36/0.3709	21.03/0.5650	27.05/0.7947	33.55/0.9194
	MH-BCS-SPL [53]	13.63/0.3177	20.63/0.5464	24.95/0.7399	29.63/0.8720	33.92/0.9380
	ISTA-Net^{++} [17]	20.89/0.5325	23.93/0.6871	26.99/0.8096	31.16/0.9067	35.81/0.9609
	SCSNet [13]	20.59/0.5123	22.25/0.6109	26.10/0.7887	27.53/0.8547	31.98/0.9383
	AMP-Net [14]	21.02/0.5367	24.27/0.7021	27.65/0.8316	32.22/0.9244	37.26/0.9704
	CSNet$^+$ [12]	20.69/0.5183	23.61/0.6729	26.41/0.7993	30.15/0.8988	34.08/0.9560
	OCTUF [18]	21.41/0.5582	25.22/0.7413	28.96/0.8608	33.68/0.9374	38.85/0.9767
	TransCS [19]	21.00/0.5288	23.74/0.6747	27.17/0.8175	30.03/0.8917	34.71/0.9572
	DPC-DUN [52]	20.91/0.5371	24.20/0.7057	27.44/0.8295	32.02/0.9262	36.99/0.9707
	CSformer [21]	21.60/0.5727	25.17/0.7478	27.96/0.8455	31.81/0.9271	35.36/0.9663
	Uformer-ICS$^+$	21.58/0.5649	25.41/0.7459	29.05/0.8573	33.83/0.9349	39.00/0.9719
	Uformer-ICS	21.94/0.5828	26.29/0.7750	30.00/0.8765	34.89/0.9421	40.33/0.9760

The best and second best PSNR and SSIM scores are highlighted in red and blue, respectively.

TABLE IV
TIME COMPLEXITY COMPARISON BETWEEN DIFFERENT CS METHODS

	Methods	PSNR (dB) / Times (s)				Scalable Sampling	Param.	FLOPs
		128×128	256×256	512×512	1024×1024			
Traditional CS methods	TV [9]	22.78/0.2059	24.62/0.6852	27.91/2.6385	32.44/9.9298	✓	-	-
	BM3D-DAMP [31]	21.67/3.3867	23.48/11.751	26.98/43.948	34.54/174.35	✓	-	-
	MH-BCS-SPL [53]	22.89/0.6402	25.14/2.9934	29.70/20.629	38.26/108.15	✓	-	-
	BCS-FOCUSS [11]	22.63/1.2723	24.61/2.3107	28.78/7.4328	36.71/29.856	✓	-	-
Deep learning-based CS methods	CSNet^{+} [12]	24.91/**0.0011**	27.17/**0.0014**	32.33/**0.0012**	40.92/**0.0016**	×	0.89M	24.26
	SCSNet [13]	24.26/0.0015	26.31/0.0012	31.06/0.0016	42.33/0.0018	✓	1.98M	12.26
	ISTA-Net^{++} [17]	24.97/0.0091	27.37/0.0091	32.64/0.0091	40.35/0.0114	✓	1.70M	50.15
	AMP-Net [14]	25.32/0.0063	27.83/0.0063	33.33/0.0071	41.34/0.0094	×	0.86M	25.77
	OCTUF [18]	25.35/0.0212	28.15/0.0218	34.11/0.0235	43.68/0.0600	×	0.55M	21.73
	TransCS [19]	24.81/0.0216	27.04/0.0214	32.27/0.0237	39.12/0.0274	×	1.75M	32.72
	DPC-DUN [52]	25.33/0.0097	27.85/0.0092	33.45/0.0096	42.05/0.0117	×	0.92M	42.67
	CSformer [21]	25.17/0.0128	27.65/0.0121	33.27/0.0131	42.88/0.0158	×	6.67M	20.82
	Uformer-ICS^{+}	25.62/0.0252	28.56/0.0243	34.85/0.0292	44.63/0.0316	✓	9.82M	49.83
	Uformer-ICS	**25.62**/0.0253	**28.75**/0.0242	**35.23**/0.0273	**45.46**/0.0320	×	9.15M	45.60

The average PSNR scores and running times are listed for different image sizes, and the FLOPs is measured on an image of size 256×256.

operation and skip connection have little difference on Set11 and Urban100, but the concatenation operation leads to a little better reconstruction performance on the whole. This is because the concatenation operation is more beneficial to generalization ability since it allows for more information preservation. In the following sections, we use the concatenation operation for feature fusion by default.

4) Loss Function: Our loss function contains three parts $\mathcal{L}_1$, $\mathcal{L}_2$ and $\mathcal{L}_3$. Besides two necessary loss items $\mathcal{L}_1$ and $\mathcal{L}_3$, $\mathcal{L}_2$ is a regularization term to ensure cycle consistency. To test the effectiveness of $\mathcal{L}_2$, we discard it in the training process and evaluate the performance. As can be seen from the settings (c) and (d) in Table II, the loss item $\mathcal{L}_2$ does benefit the reconstruction performance in most cases. Specifically, when the sampling ratio is larger than 0.1, the PSNR scores with $\mathcal{L}_2$ can improve by approximately 0.06$\sim$0.71 dB and 0.21$\sim$0.24 dB on Set11 and Urban100 datasets, respectively.

C. Performance Evaluation

We compare the proposed method with other CS methods in terms of the quantitative results, visual results, and model complexity. The PSNR and structural similarity index measure (SSIM) scores are used to quantitatively evaluate the reconstruction quality.

1) Quantitative Comparison: We calculate the average PSNR and SSIM scores on the five testing datasets at the sampling ratios ranging from 0.01–0.5. Table III lists the experimental results for all competing CS methods. Benefiting from the powerful learning ability, all deep learning-based CS methods outperform the traditional CS methods. The proposed method achieves the best PSNR and SSIM scores for nearly all the sampling ratios. Specifically, the proposed Uformer-ICS can obtain significantly higher PSNR scores than other deep learning-based methods on the Urban100 dataset, which contains high-resolution images with different characteristics. The proposed Uformer-ICS can also achieve the best SSIM scores when the sampling ratio is smaller than 0.5.

Additionally, we also calculate the average PSNR scores over all the five testing datasets at all sampling ratios, and the results of these deep learning-based CS methods are shown in Fig. 1. It is evident that the proposed method achieve significantly higher scores than other deep learning-based methods for all sampling ratios. The quantitative comparison results presented in Table III and Fig. 1 indicate that the proposed method outperforms all other CS methods and has a better generalization ability for different datasets.

Regarding scalable sampling and reconstruction ability, the proposed Uformer-ICS^{+} requires only one-time training but can sample and reconstruct images at arbitrary sampling ratios. Compared with the scalable CS methods SCSNet and ISTA-Net^{++}, the proposed Uformer-ICS^{+} can still obtain better PSNR and SSIM scores in most cases. For the test datasets Set14 and BSD100, the proposed Uformer-ICS^{+} achieve the best PSNR scores compared to all other non-scalable deep learning-based CS methods. These comparison results demonstrate the tremendous potential of the proposed method for scalable sampling and reconstruction.

2) Visual Comparison: Fig. 8 shows the visual results of different CS methods at the sampling ratios of 0.04 and 0.1, where "Ours-Non-Adaptive" refers to the version of our Uformer-ICS without the adaptive sampling module. The reconstruction results of all the traditional CS methods clearly show blocking artifacts, whereas those of the deep learning-based CS methods show significantly fewer blocking artifacts. Moreover, the visual results demonstrate that the proposed Uformer-ICS can recover more image details and clearer edges than other deep learning-based CS methods. For example, the reconstructed images of our Uformer-ICS exhibit more details around the letter area in the "ppt3" and "img-076" images. This is because the proposed sampling model uses an adaptive sampling strategy to allocate more sampling resources to the image block that has less sparsity, and the proposed reconstruction model can

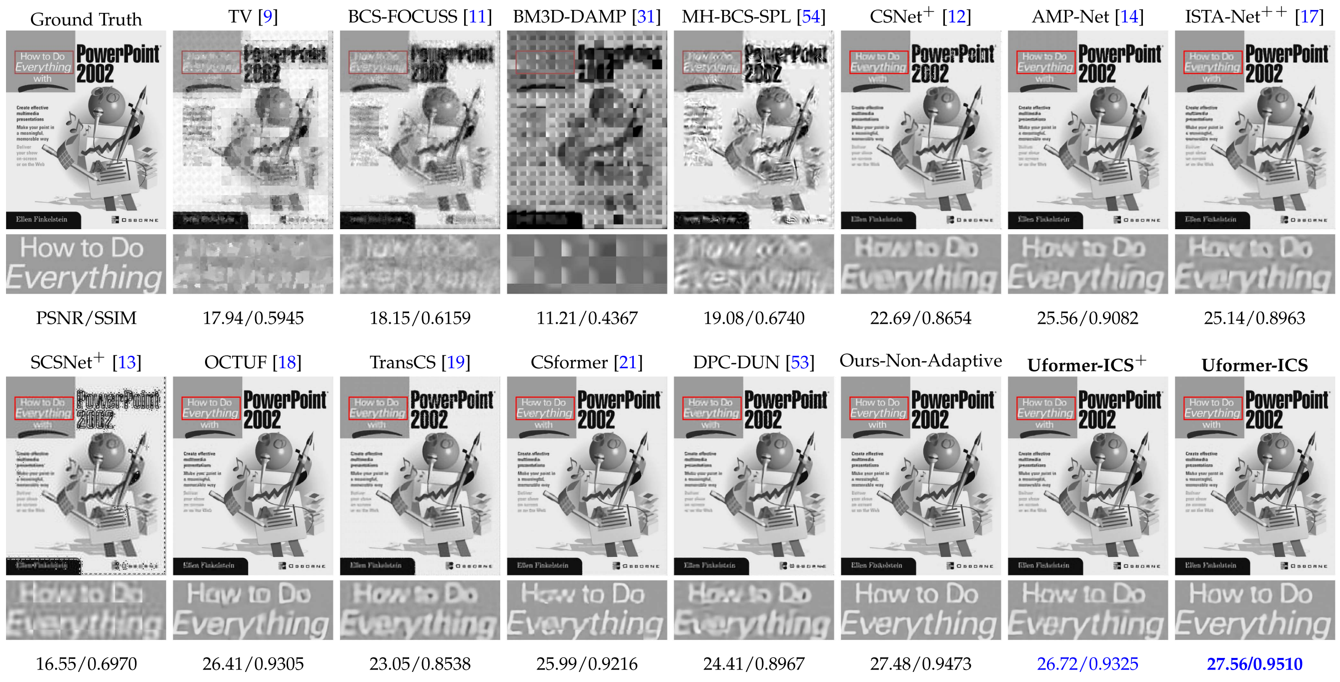

(a) Reconstruction results of the image "ppt3" at sr = 0.04

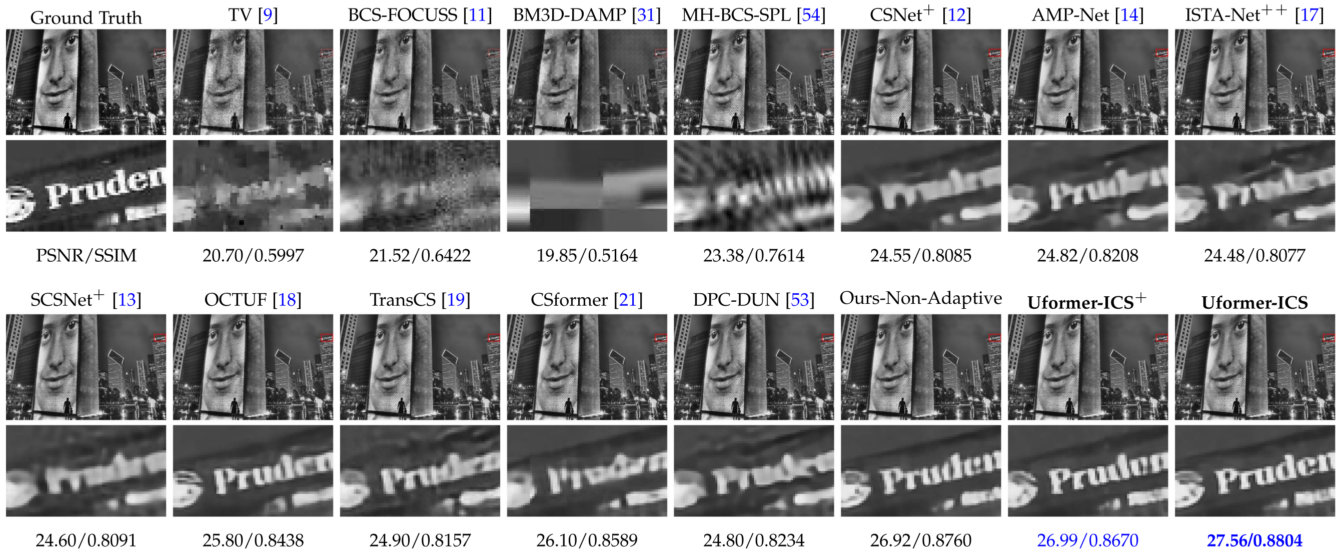

(b) Reconstruction results of the image "img-076" at sr = 0.1

Fig. 8. Reconstruction results of various CS methods at sampling ratios (srs) of 0.04 and 0.1. Note that "Ours-Non-Adaptive" refers to the version of our Uformer-ICS without adaptive sampling module.

simultaneously capture the long-range dependency and local features of the image to reconstruct image information.

D. Model Complexity

We test the average running times on different image resolutions to evaluate the actual reconstruction efficiencies of all competing CS methods. Specifically, we randomly select five images from the ImageNet validation dataset and resize them to 128×128, 256×256, 512×512, and 1024×1024 using the bicubic interpolation algorithm. Thereafter, the average running times are calculated for the five images using these four kinds of image resolutions. Additionally, we utilize the number of floating-point operations (FLOPs) and parameters to theoretically quantify the time complexity of deep learning-based CS methods. It should be noted that we calculate the FLOPs on an input image of size 256×256, and evaluate all the models at the sampling ratio of 0.25. The traditional CS methods are tested on the CPU device, whereas the deep learning-based CS methods are tested on the GPU device.

Table IV presents the comparison results of model complexity. As can be seen, traditional CS methods have much lower reconstruction quality and significantly lower running speeds, which may not satisfy the high-efficiency requirement of real-time applications. For example, they all cost more than two seconds to reconstruct the image of size 512×512. All deep learning-based CS methods have better PSNR scores and extremely faster speeds than traditional ones. Moreover, the running speeds of all deep learning-based CS methods are of the same order of magnitude. This is because the GPU device has a powerful computational ability and can run these deep learning-based models at high speed. The proposed method can achieve the best PSNR scores for all the image resolutions. Additionally, the Uformer-ICS$^+$ uses a single model for arbitrary sampling and reconstruction tasks, which can significantly reduce the number of parameters when sampling at multiple sampling ratios is required. Thus, the proposed method can well balance the trade-off between model complexity and reconstruction performance. It achieves the best reconstruction performance while maintaining a modest model complexity.

V. Conclusion

In this article, we proposed a novel transformer-based network for image CS, called Uformer-ICS, which effectively introduces two CS characteristics into the transformer architecture. We first designed an adaptive sampling architecture to retain the maximum possible information of the original image under a fixed sampling ratio. Specifically, it estimates sparsity from image measurements and linearly allocates measurement resources based on the estimated block sparsity. We utilized three sparsity estimation methods to evaluate the adaptive sampling architecture. Besides, we designed a MCP module to adapt the projection operation into the multi-channel feature domain. We constructed the projection-based transformer block by integrating the MCP module into the original transformer block and then built a symmetrical reconstruction model using the projection-based transformer blocks and residual convolutional blocks. Experimental results verified the effectiveness of the proposed Uformer-ICS, demonstrated its superiority over existing deep learning-based CS methods, and proved its tremendous potential for scalable sampling and reconstruction.

References

[1] A. Kaur, N. Auluck, and O. Rana, "Real-time scheduling on hierarchical heterogeneous fog networks," *IEEE Trans. Serv. Comput.*, vol. 16, no. 2, pp. 1358–1372, Mar./Apr. 2023.

[2] J. Li, W. Liang, W. Xu, Z. Xu, Y. Li, and X. Jia, "Service home identification of multiple-source IoT applications in edge computing," *IEEE Trans. Serv. Comput.*, vol. 16, no. 2, pp. 1417–1430, Mar./Apr. 2023.

[3] E. J. Candès, J. Romberg, and T. Tao, "Robust uncertainty principles: Exact signal reconstruction from highly incomplete frequency information," *IEEE Trans. Inf. Theory*, vol. 52, no. 2, pp. 489–509, Feb. 2006.

[4] D. L. Donoho, "Compressed sensing," *IEEE Trans. Inf. Theory*, vol. 52, no. 4, pp. 1289–1306, Apr. 2006.

[5] X. Yuan, D. J. Brady, and A. K. Katsaggelos, "Snapshot compressive imaging: Theory, algorithms, and applications," *IEEE Signal Process. Mag.*, vol. 38, no. 2, pp. 65–88, Mar. 2021.

[6] J. Yao, X. Liu, X. Zhu, and H. Guan, "Control of large-scale systems through dimension reduction," *IEEE Trans. Serv. Comput.*, vol. 8, no. 4, pp. 563–575, Jul./Aug. 2015.

[7] L. Gong, K. Qiu, C. Deng, and N. Zhou, "An optical image compression and encryption scheme based on compressive sensing and RSA algorithm," *Opt. Lasers Eng.*, vol. 121, pp. 169–180, 2019.

[8] A. Beck and M. Teboulle, "A fast iterative shrinkage-thresholding algorithm for linear inverse problems," *SIAM J. Imag. Sci.*, vol. 2, no. 1, pp. 183–202, 2009.

[9] C. Li, W. Yin, and Y. Zhang, "User's guide for TVAL3: TV minimization by augmented lagrangian and alternating direction algorithms," *CAAM Rep.*, vol. 20, no. 46/47, pp. 4, 2009.

[10] L. Gan, "Block compressed sensing of natural images," in *Proc. 15th Int. Conf. Digit. Signal Process.*, 2007, pp. 403–406.

[11] A. S. Unde and P. Deepthi, "Block compressive sensing: Individual and joint reconstruction of correlated images," *J. Vis. Commun. Image Representation*, vol. 44, pp. 187–197, 2017.

[12] W. Shi, F. Jiang, S. Liu, and D. Zhao, "Image compressed sensing using convolutional neural network," *IEEE Trans. Image Process.*, vol. 29, pp. 375–388, 2020.

[13] W. Shi, F. Jiang, S. Liu, and D. Zhao, "Scalable convolutional neural network for image compressed sensing," in *Proc. IEEE/CVF Conf. Comput. Vis. Pattern Recognit.*, 2019, pp. 12282–12291.

[14] Z. Zhang, Y. Liu, J. Liu, F. Wen, and C. Zhu, "AMP-net: Denoising-based deep unfolding for compressive image sensing," *IEEE Trans. Image Process.*, vol. 30, pp. 1487–1500, 2021.

[15] Y. Sun, J. Chen, Q. Liu, B. Liu, and G. Guo, "Dual-path attention network for compressed sensing image reconstruction," *IEEE Trans. Image Process.*, vol. 29, pp. 9482–9495, 2020.

[16] J. Zhang, C. Zhao, and W. Gao, "Optimization-inspired compact deep compressive sensing," *IEEE J. Sel. Topics Signal Process.*, vol. 14, no. 4, pp. 765–774, May 2020.

[17] D. You, J. Xie, and J. Zhang, "ISTA-NET: Flexible deep unfolding network for compressive sensing," in *Proc. IEEE Int. Conf. Multimedia Expo*, 2021, pp. 1–6.

[18] J. Song, C. Mou, S. Wang, S. Ma, and J. Zhang, "Optimization-inspired cross-attention transformer for compressive sensing," in *Proc. IEEE/CVF Conf. Comput. Vis. Pattern Recognit.*, 2023, pp. 6174–6184.

[19] M. Shen, H. Gan, C. Ning, Y. Hua, and T. Zhang, "TransCS: A transformer-based hybrid architecture for image compressed sensing," *IEEE Trans. Image Process.*, vol. 31, pp. 6991–7005, 2022.

[20] H. Gan, M. Shen, Y. Hua, C. Ma, and T. Zhang, "From patch to pixel: A transformer-based hierarchical framework for compressive image sensing," *IEEE Trans. Comput. Imag.*, vol. 9, pp. 133–146, 2023.

[21] D. Ye, Z. Ni, H. Wang, J. Zhang, S. Wang, and S. Kwong, "CSformer: Bridging convolution and transformer for compressive sensing," *IEEE Trans. Image Process.*, vol. 32, pp. 2827–2842, 2023.

[22] A. Vaswani et al., "Attention is all you need," in *Proc. Adv. Neural Inf. Process. Syst.*, 2017, pp. 6000–6010.

[23] T. Xiao et al., "Loader: A log anomaly detector based on transformer," *IEEE Trans. Serv. Comput.*, vol. 16, no. 5, pp. 3479–3492, Sep./Oct. 2023.

[24] S. Yu, P. He, N. Chen, and Y. Wu, "Brain: Log parsing with bidirectional parallel tree," *IEEE Trans. Serv. Comput.*, vol. 16, no. 5, pp. 3224–3237, Sep./Oct. 2023.

[25] J. Liang, J. Cao, G. Sun, K. Zhang, L. Van Gool, and R. Timofte, "SwinIR: Image restoration using swin transformer," in *Proc. IEEE/CVF Int. Conf. Comput. Vis.*, 2021, pp. 1833–1844.

[26] A. Dosovitskiy et al., "An image is worth 16x16 words: Transformers for image recognition at scale," 2020, *arXiv:2010.11929*.

[27] D. L. Donoho, A. Maleki, and A. Montanari, "Message-passing algorithms for compressed sensing," *Proc. Nat. Acad. Sci. USA*, vol. 106, no. 45, pp. 18914–18919, 2009.

[28] Y. Yu, B. Wang, and L. Zhang, "Saliency-based compressive sampling for image signals," *IEEE Signal Process. Lett.*, vol. 17, no. 11, pp. 973–976, Nov. 2010.

[29] J. E. Fowler, S. Mun, and E. W. Tramel, "Multiscale block compressed sensing with smoothed projected landweber reconstruction," in *Proc. 19th Eur. Signal Process. Conf.*, 2011, pp. 564–568.

[30] J. Chen, X. Zhang, and H. Meng, "Self-adaptive sampling rate assignment and image reconstruction via combination of structured sparsity and non-local total variation priors," *Digit. Signal Process.*, vol. 29, pp. 54–66, Jun. 2014.

[31] C. A. Metzler, A. Maleki, and R. G. Baraniuk, "From denoising to compressed sensing," *IEEE Trans. Inf. Theory*, vol. 62, no. 9, pp. 5117–5144, Sep. 2016.

[32] Z. Liu et al., "Swin transformer: Hierarchical vision transformer using shifted windows," Aug. 2021, *arXiv:2103.14030*.

[33] S. W. Zamir, A. Arora, S. Khan, M. Hayat, F. S. Khan, and M.-H. Yang, "Restormer: Efficient transformer for high-resolution image restoration," 2021, *arXiv:2111.09881*.

[34] A. Mousavi, A. B. Patel, and R. G. Baraniuk, "A deep learning approach to structured signal recovery," in *Proc. 53rd Annu. Allerton Conf. Commun. Control Comput.*, 2015, pp. 1336–1343.

[35] K. Kulkarni, S. Lohit, P. Turaga, R. Kerviche, and A. Ashok, "ReconNet: Non-iterative reconstruction of images from compressively sensed measurements," in *Proc. IEEE Conf. Comput. Vis. Pattern Recognit.*, 2016, pp. 449–458.

[36] W. Shi, F. Jiang, S. Zhang, and D. Zhao, "Deep networks for compressed image sensing," in *Proc. IEEE Int. Conf. Multimedia Expo*, 2017, pp. 877–882.

[37] J. Zhang and B. Ghanem, "ISTA-net: Interpretable optimization-inspired deep network for image compressive sensing," in *Proc. IEEE Conf. Comput. Vis. Pattern Recognit.*, 2018, pp. 1828–1837.

[38] S. Zhou, Y. He, Y. Liu, C. Li, and J. Zhang, "Multi-channel deep networks for block-based image compressive sensing," *IEEE Trans. Multimedia*, vol. 23, pp. 2627–2640, 2021.

[39] B. Chen and J. Zhang, "Content-aware scalable deep compressed sensing," *IEEE Trans. Image Process.*, vol. 31, pp. 5412–5426, 2022.

[40] K. Zhang, Z. Hua, Y. Li, Y. Chen, and Y. Zhou, "AMS-net: Adaptive multiscale network for image compressive sensing," *IEEE Trans. Multimedia*, vol. 25, pp. 5676–5689, 2022.

[41] W. Shi et al., "Real-time single image and video super-resolution using an efficient sub-pixel convolutional neural network," in *Proc. IEEE Conf. Comput. Vis. Pattern Recognit.*, 2016, pp. 1874–1883.

[42] K. He, X. Zhang, S. Ren, and J. Sun, "Deep residual learning for image recognition," in *Proc. IEEE Conf. Comput. Vis. Pattern Recognit.*, 2016, pp. 770–778.

[43] O. Ronneberger, P. Fischer, and T. Brox, "U-net: Convolutional networks for biomedical image segmentation," in *Proc. Int. Conf. Med. Image Comput. Comput.- Assist. Intervention*, 2015, pp. 234–241.

[44] J. L. Ba, J. R. Kiros, and G. E. Hinton, "Layer normalization," 2016, *arXiv:1607.06450*.

[45] J.-Y. Zhu, T. Park, P. Isola, and A. A. Efros, "Unpaired image-to-image translation using cycle-consistent adversarial networks," in *Proc. IEEE Int. Conf. Comput. Vis.*, 2017, pp. 2223–2232.

[46] T.-Y. Lin et al., "Microsoft COCO: Common objects in context," in *Proc. Eur. Conf. Comput. Vis.*, 2014, pp. 740–755.

[47] M. Bevilacqua, A. Roumy, C. Guillemot, and M. Line Alberi Morel, "Low-complexity single-image super-resolution based on nonnegative neighbor embedding," in *Proc. Brit. Mach. Vis. Conf.*, 2012, pp. 135.1–135.10.

[48] R. Zeyde, M. Elad, and M. Protter, "On single image scale-up using sparse-representations," in *Proc. Curves Surfaces*, 2012, pp. 711–730.

[49] D. Martin, C. Fowlkes, D. Tal, and J. Malik, "A database of human segmented natural images and its application to evaluating segmentation algorithms and measuring ecological statistics," in *Proc. IEEE 8th Int. Conf. Comput. Vis.*, 2001, pp. 416–423.

[50] J.-B. Huang, A. Singh, and N. Ahuja, "Single image super-resolution from transformed self-exemplars," in *Proc. IEEE Conf. Comput. Vis. Pattern Recognit.*, 2015, pp. 5197–5206.

[51] D. P. Kingma and J. Ba, "Adam: A method for stochastic optimization," 2014, *arXiv:1412.6980*.

[52] J. Song, B. Chen, and J. Zhang, "Dynamic path-controllable deep unfolding network for compressive sensing," *IEEE Trans. Image Process.*, vol. 32, pp. 2202–2214, 2023.

[53] C. Chen, E. W. Tramel, and J. E. Fowler, "Compressed-sensing recovery of images and video using multihypothesis predictions," in *Proc. Conf. Rec. 45th Asilomar Conf. Signals Syst. Comput.*, 2011, pp. 1193–1198.

Kuiyuan Zhang received the MS degree in computer science and technology from the Harbin Institute of Technology, Shenzhen, China. He is currently working toward the PhD degree in computer science and technology with the Harbin Institute of Technology, Shenzhen, China. His current research interests include image compressive sensing, image encryption and multimedia deepfake detection.

Zhongyun Hua (Senior Member, IEEE) received the BS degree in software engineering from Chongqing University, Chongqing, China, in 2011, and the MS and PhD degrees in software engineering from the University of Macau, Macau, China, in 2013 and 2016, respectively. He is currently an associate professor with the School of Computer Science and Technology, Harbin Institute of Technology, Shenzhen, China. His works have appeared in prestigious venues such as *IEEE Transactions on Dependable and Secure Computing, IEEE Transactions on Computers, IEEE Transactions on Signal Processing, IEEE Transactions on Image Processing, IEEE Transactions on Systems, Man, and Cybernetics: Systems*, and *ACM MultiMedia*. His current research interests are focused on chaotic system, multimedia security, and secure cloud computing. He has published more than 80 papers on the subject, receiving more than 5000 citations. He has been recognized as a 'Highly Cited Researcher 2023' and 'Highly Cited Researcher 2022'. He is currently an associate editor for *International Journal of Bifurcation and Chaos*.

Yuanman Li (Member, IEEE) received the BEng degree in software engineering from Chongqing University, Chongqing, China, in 2012, and the PhD degree in computer science from the University of Macau, Macau, in 2018. From 2018 to 2019, he was a post-doctoral fellow with the State Key Laboratory of Internet of Things for Smart City, University of Macau. He is currently an assistant professor with the College of Electronics and Information Engineering, Shenzhen University, Shenzhen, China. His current research interests include data representation, multimedia security and forensics, computer vision, and machine learning.

Yushu Zhang (Senior Member, IEEE) received the BS degree from the School of Science, North University of China, Taiyuan, China, in 2010, and the PhD degree from the College of Computer Science and Technology, Chongqing University, Chongqing, China, in 2014. He held various research positions with the City University of Hong Kong, Southwest University, the University of Macau, and Deakin University. He is currently a professor with the College of Computer Science and Technology, Nanjing University of Aeronautics and Astronautics, China. His research interests include multimedia security, blockchain, and artificial intelligence security. He is an associate editor of *Information Sciences*, *Journal of King Saud University-Computer and Information Sciences*, and *Signal Processing*.

Yicong Zhou (Senior Member, IEEE) received the BS degree in electrical engineering from Hunan University, Changsha, China, in 1992, and the MS and PhD degrees in electrical engineering from Tufts University, Medford, Massachusetts, in 2008 and 2010, respectively. He is a professor with the Department of Computer and Information Science, University of Macau, Macau, China. His research interests include image processing, computer vision, machine learning, and multimedia security. He was recognized as one of the World's Top 2% Scientists and one of the Highly Cited Researchers, in 2020 and 2021. He received the Third Price of Macao Natural Science Award as a sole winner, in 2020 and was a co-recipient, in 2014. He has been a leading co-chair of the Technical Committee on Cognitive Computing of the IEEE Systems, Man, and Cybernetics Society since 2015. He serves as an associate editor for *IEEE Transactions on Neural Networks and Learning Systems, IEEE Transactions on Circuits and Systems for Video Technology*, and *IEEE Transactions on GeoScience and Remote Sensing*.